# Comparison of scrape-off layer turbulence in Alcator C-Mod with three dimensional gyrofluid computations

S. J. Zweben,[1] B. D. Scott,[2] J. L. Terry,[3] B. LaBombard,[3] J. W. Hughes,[3] and D. P. Stotler[1]
[1]*Princeton Plasma Physics Laboratory, Princeton, New Jersey 08540, USA*
[2]*Max-Planck-Institute fur Plasmaphysik, Euratom Association, D-85748 Garching, Germany*
[3]*Massachusetts Institute of Technology, Cambridge, Massachusetts 02139, USA*

(Received 8 April 2009; accepted 8 July 2009; published online 18 August 2009)

This paper describes quantitative comparisons between turbulence measured in the scrape-off layer (SOL) of Alcator C-Mod [S. Scott, A. Bader, M. Bakhtiari *et al.*, Nucl. Fusion **47**, S598 (2007)] and three dimensional computations using electromagnetic gyrofluid equations in a two-dimensional tokamak geometry. These comparisons were made for the outer midplane SOL for a set of inner-wall limited, near-circular Ohmic plasmas. The $B$ field and plasma density were varied to assess gyroradius and collisionality scaling. The poloidal and radial correlation lengths in the experiment and computation agreed to within a factor of 2 and did not vary significantly with either $B$ or density. The radial and poloidal propagation speeds and the frequency spectra and poloidal $k$-spectra also agreed fairly well. However, the autocorrelation times and relative $D_a$ fluctuation levels were higher in the experiment by more than a factor of 2. Possible causes for these disagreements are discussed. © *2009 American Institute of Physics*. [DOI: 10.1063/1.3191721]

## I. INTRODUCTION

Turbulence in the scrape-off layer (SOL) of tokamaks is not yet understood in terms of theory or computational models. The goal of this paper is to make a quantitative comparison between turbulence measured in the SOL of Alcator C-Mod (Ref. 1) and computational simulations based on the GEMR model.[2] This is done by using C-Mod discharges which are appropriate for GEMR analysis, and by comparing experimental and modeling results using the same analysis tools.

The turbulence measured in this experiment is qualitatively similar to SOL turbulence measured in many other tokamaks, as reviewed previously in Ref. 3. For example, the spectra are broadband (~10–100 kHz), the correlation lengths perpendicular to $B$ are short (~1 cm or $\sim 50\rho_s$), and the fluctuation levels are high (~10–50%). The new aspect of the present measurements is their direct comparison with the GEMR turbulence modeling, which was done (as far as possible) to match these specific experiments in C-Mod.

Only a few previous direct comparisons have been made between SOL turbulence measurements and edge turbulence simulations, e.g., using the ESEL code for the TCV tokamak and JET,[4] the BOUT code for Alcator C-Mod,[5] and the SOLT code for NSTX.[6] Comparisons of core plasma turbulence with turbulence simulations also have been done previously, e.g., for DIII-D using the GYRO code,[7] and for the TJ-K torsatron using the GEM3 code.[8] In general, there is still no clear quantitative understanding of the SOL turbulence or turbulence-induced transport, so relevant theory is still in the process of development.[9–12]

The GEMR code used for this paper is described in Ref. 2. It uses three dimensional (3D) electromagnetic gyrofluid equations in a "$\delta$-$f$" limit[13] and a two dimensional (2D) global description of tokamak geometry on field aligned coordinates.[14] The "$\delta$-$f$" limit refers to the use of equations based on local parameters. The gradient, however, evolves freely in the presence of sources and sinks, ultimately describing a saturated profile. The input parameters are taken from a point in the middle of the Alcator C-Mod SOL and the saturated turbulence is compared to measurements just outside this position. Thus the GEMR model does *not* attempt to simulate the actual radial profile of the edge or SOL of C-Mod, but rather attempts to simulate the turbulence in a single radial region of the SOL in a self-consistent manner.

Section II describes the C-Mod plasma conditions and diagnostics used for this experiment and Sec. III describes GEMR and its application to this experiment. Section IV contains the comparisons between the measurements and the model and Sec. V is a discussion of the results and a summary of the limitations and uncertainties of this comparison.

## II. PLASMA CONDITIONS AND DIAGNOSTICS

This section describes the plasma conditions and diagnostics used for the measurements in this paper. The plasmas parameters were well within the normal range of C-Mod operation and the diagnostics were the standard C-Mod Langmuir probes and gas puff imaging (GPI) systems. The comparisons between experiment and model are done only for the outer midplane SOL region of C-Mod.

### A. Plasma and SOL parameters

The plasmas used for this experiment were chosen to match the computational capabilities of the GEMR model. Since the GEMR model does not incorporate divertor geometry, this experiment was done using an inner-wall limited, nearly circular (plasma elongation $\kappa \sim 1.2$), deuterium Ohmic plasma. The only unusual feature of these plasmas was a relatively large outer midplane "gap" of ~3.8 cm be-

 

TABLE I. Plasma and SOL parameters for this experiment.

| $B_o$ (T) | $I$ (*MA*) | $\langle n_e \rangle / 10^{14}$ (cm$^{-3}$) | No. of shots |
|---|---|---|---|
| 2.9 | 0.4 | 0.84–1.36 | 10 |
| 4.1 | 0.6 | 1.36–2.02 | 4 |
| 5.4 | 0.8 | 1.56–2.51 | 8 |

tween the last closed flux surface and the outer midplane limiter, to allow improved diagnostic access to the outer midplane SOL.

The main external variables in this experiment were the toroidal field and the line-averaged plasma density, which varied as shown in Table I. The toroidal field ranged from $B_o$=2.9–5.4 T (at $R_o$=67 cm), with a nearly constant $q(a) \sim 3$. For each $B$ the density was varied as much as possible using variable gas puffing, but it was always well below the Greenwald limit, i.e., $n/n_G \sim 0.3$–$0.5$. For all cases the last closed flux surface was at $R$=86.7 cm and the outer limiter was at $R$=90.5 cm. Two runs were done (Shot Nos. 1070504001-11 and 1070801015-35) with a total of 22 discharges in the final database. As can be seen from Table I, there was a trend for $\langle n_e \rangle$ to be higher at higher magnetic fields and plasma currents in these Ohmic discharges, so it is not easy to isolate the effects of these two variables.

Figure 1 shows the time dependence of the basic plasma parameters in this experiment. The global plasma conditions were nearly constant from ~0.7–1.3 s and time of interest for the turbulence comparisons was near the peak of the GPI

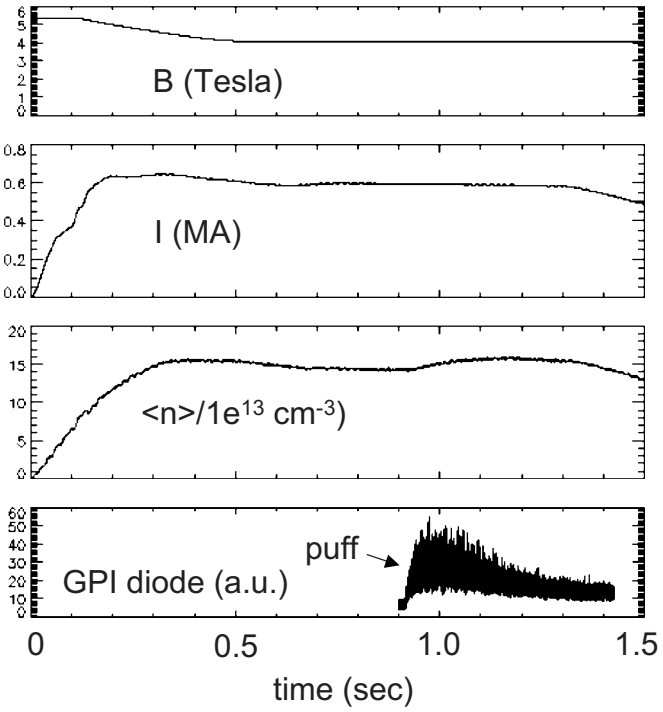


FIG. 1. Time dependence of the plasmas in this experiment for a typical case ($B_o$=4.0 T, Shot No. 1070801024). The magnetic field, plasma current, and line-averaged density were nearly constant from ~0.7 to 1.3 ms. The GPI gas puff entered the discharge at 0.9 ms and the turbulence was measured near the peak in the GPI signal at ~1.0–1.01 s.

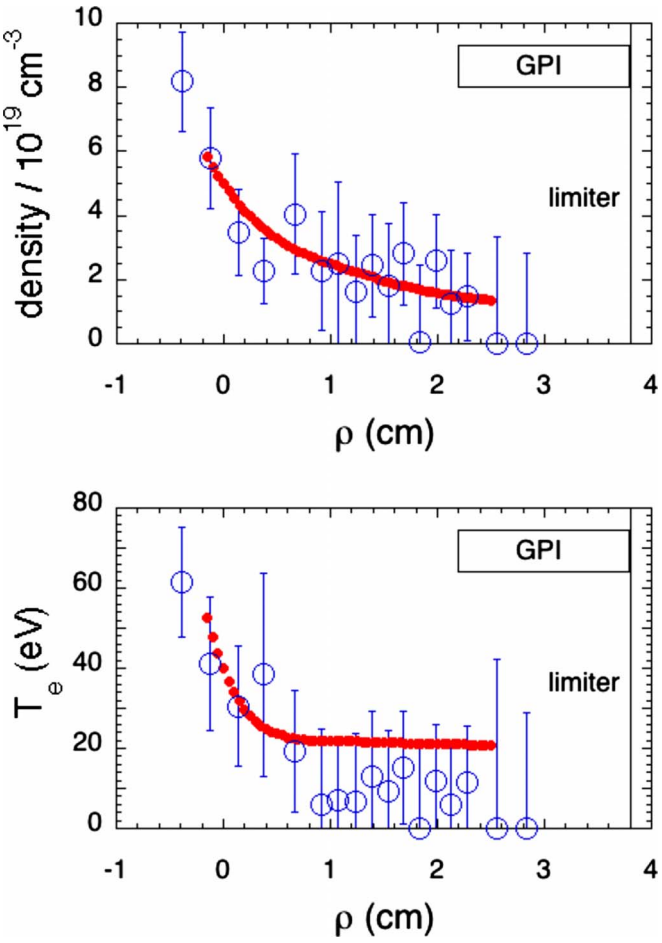


FIG. 2. (Color online) Measurements of $n_e$ and $T_e$ profiles in the SOL by the edge Thomson scattering (open circles) and Langmuir probe (dots) at ~0.9–1.0 s for the same discharge as for Fig. 1. The radial coordinate is with respect to the last closed flux surface at the outboard midplane. The solid vertical line indicates the shadow of a nearby limiter. The boxes indicate the radial region of the GPI photodiode measurements.

diagnostic gas puff, namely 1.0–1.01 s for this shot. The GPI gas puff caused a ~5%–30% increase in $\langle n_e \rangle$ for the discharges in this experiment, but there was no significant variation in the turbulence as measured over the duration of the puff from 0.92–1.1 s, i.e., as the magnitude of the puff varied.

Figure 2 shows typical measurements of the SOL profiles of density and temperature made with a reciprocating Langmuir probe and edge Thomson scattering. These profiles are plotted versus $\rho$ (the radial distance beyond from the last closed flux surface mapped to the midplane) and overlap fairly well after a ~3–5 mm radial shift was applied to align the edge Thomson scattering data with the probe data, which gives an indication of the uncertainty in the location of the last closed flux surface. The density and temperature used as input to the GEMR modeling were taken from the Langmuir probe profiles at $\rho$=1.3 cm for each case, which is outside the steep gradient region of the near-SOL. The GPI turbulence measurements were averaged over $\rho \sim 2.2$–$3.8$ cm, as shown by boxes in Fig. 2.

Since the Langmuir probe and edge Thomson scattering data were not available for all shots in this experiment, the

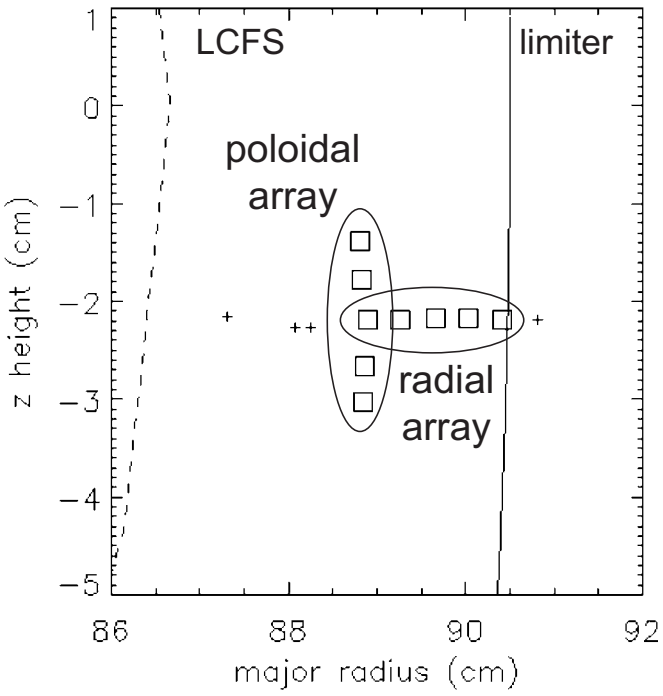


FIG. 3. Location of the radial and poloidal arrays of the GPI photodiode views for this experiment. Each symbol is the center of a sightline which has an ~0.3 cm diameter at the GPI gas puff. The five large squares in the poloidal array were used for the poloidal measurements and the five large squares in the radial array were used for the radial measurements. The EFIT estimate of the LCFS is shown by the dashed line and the outer limiter radius is shown by the solid line.

scaling of the turbulence results with density was done using the line-averaged density $\langle n_e \rangle$. The line-averaged density was approximately proportional to the local density near the last closed flux surface in the cases in which that was measured, so is a reasonable proxy for the local value.

### B. Gas puff imaging diagnostic

The GPI diagnostic on C-Mod has been described previously.[15] The SOL turbulence was measured by the fluctuations in the $D_\alpha$ light emitted by a localized neutral deuterium gas puff near the outer midplane. The GPI viewing system used for this paper was a discrete set of fast photodiodes viewing the GPI puff toroidally over two separate linear arrays of views, one radial array and one vertical/poloidal array, as shown in Fig. 3. Each point in Fig. 3 represents the center of a sightline with a viewing diameter of ~0.3 cm at the GPI puff. The large square symbols are the diode views used for comparison with GEMR results and the small crosses are four additional radial views used for profile measurements in Sec. III D.

The signals from each detector were digitized at 1 MHz and had an effective bandwidth of ~0.4 MHz. Results from the five detectors in the poloidal array were averaged for the poloidal measurements and the results from five neighboring detectors in the radial array were averaged for the radial measurements. The additional radial detectors did not have a high enough signal/noise level for correlation analyses.

### C. DEGAS-2 modeling of the GPI spatial resolution

To make a direct comparison between the GPI measurements and the GEMR model, the density and temperature fluctuations from the GEMR model were first converted into $D_\alpha$ light fluctuations and then space- and time-averaged to simulate the measured instrumental resolution of the GPI detectors.

Due to the ~8° angle between the toroidally viewing sightlines of the present GPI photodiode detectors and the local $B$ field lines (along which the local turbulence structure is assumed to be constant), there was a spatial averaging over the finite toroidal extent of the GPI gas cloud, which was not directly measured. This additional spatial averaging was estimated from the 3D DEGAS-2 neutral transport/atomic physics model[16] using the measured GPI gas nozzle geometry and measured SOL plasma parameters. The calculated toroidal extent of the $D_\alpha$ emission cloud was ~6 cm full width at half maximum (FWHM), which results in an additional *poloidal* averaging of ~0.8 cm FWHM. This is significantly larger than the 0.3 cm viewing diameter of the GPI sightline, so this gas cloud effect dominates the poloidal spatial resolution of the GPI system in this experiment. However, the *radial* averaging due to this effect is <0.1 cm, which is negligible compared with the diameter of the GPI sightline.

### D. Radial profiles of turbulence in the SOL

Since GEMR is a "local" turbulence model, it calculates the turbulence for a single radial region of the SOL and does not calculate the radial profile of the turbulence in the SOL. Therefore the comparisons in this paper between the GPI measurements and GEMR results do not take into account the radial dependence of the turbulence in the SOL, but use only averages over the GPI arrays shown in Fig. 3.

To help assess the uncertainty introduced by this averaging, Fig. 4 shows a typical profile of all nine radial diodes for a few of the turbulence quantities measured in this experiment, including shot-to-shot error bars. The shaded region corresponds to the five radial diode views, which were averaged over for comparison with the GEMR results. For these cases the $L_{\mathrm{rad}}$ and $\tau_{\mathrm{auto}}$ profiles are roughly flat across the shaded region (see Sec. IV for definitions), so their average is a good estimate for the mid-SOL. However, the $D_\alpha$ fluctuation level increases with radius, as seen in previous experiments,[3] so the average of the relative $D_\alpha$ fluctuation level is a more uncertain estimate of a mid-SOL value.

The poloidal profiles of the turbulence are typically constant to within ±10% over the range of the poloidal array views in Fig. 3, which is comparable to the shot-to-shot variability. However, over the ~4 cm range of the full 12 photodiode poloidal array there was a systematic trend for the poloidal correlation length and autocorrelation time to increase with increasing height ($z$) and for the relative $D_\alpha$ fluctuation level to decrease with increasing $z$. These trends are qualitatively consistent with the expected systematic changes due to the varying the angle between the detector sightlines and the local $B$ field lines. Therefore the five poloidal GPI

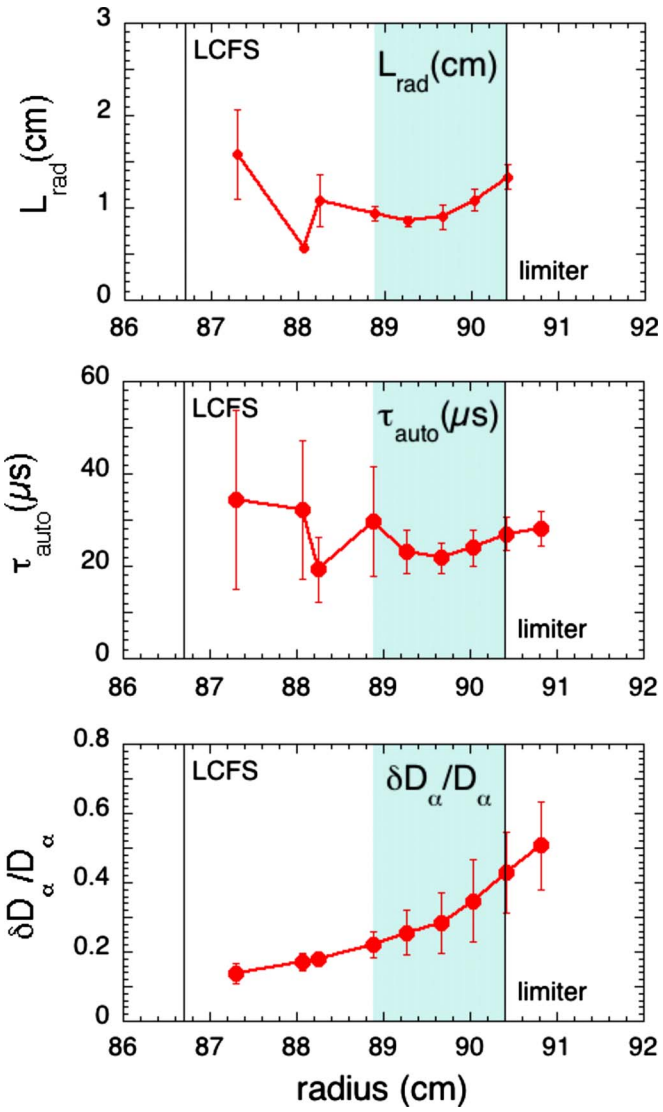


FIG. 4. (Color online) Typical radial profiles of a few of the turbulence characteristics measured by GPI in the SOL of C-Mod for the four $B_o$=4.0 T cases. The shaded box indicates the region over which the GPI data are averaged for the comparisons with GEMR. The radial correlation lengths and autocorrelation times are approximately independent of radius over the shaded region, but the relative $D_\alpha$ fluctuation level increases with radius (as seen in other tokamaks). The error bars are shot-to-shot variations.

views in Fig. 3 were chosen since they had the nearest $z$ and field line angle to the radial array and so could use the same poloidal smoothing correction.

## III. GEMR MODELING OF THE C-MOD SOL

The turbulence computations for this paper were done with a global model of gyrofluid turbulence called GEMR—GEM is a gyrofluid electromagnetic model for electrons and ions and the "R" refers to the use of global, radially dependent, geometry. For a detailed description of the GEM model, see, for example, Ref. 13, for the description of the geometry see Sec. V of Ref. 14, and for the implementation into a time-dependent self-consistent, radially varying geometry see Secs. 2 and 3 of Ref. 2. The sum of these references constitutes the basis of the GEMR code. For recent discussions of computational edge turbulence, see Refs. 9 and 12 for varying points of view.

### A. Basic equations and assumptions

The GEM model is a "$\delta$-$f$" formulation of the gyrofluid equations in an electromagnetic setting. Shear Alfvén dynamics is kept, while compressional Alfvén dynamics is not. Six moment variables (density, parallel velocity, parallel and perpendicular temperatures, and parallel/parallel and perpendicular/parallel components of the heat flux) are kept as dependent variables and advanced in time. The full set is carried for both ions and electrons. At each time step the field equations (gyrofluid versions of the gyrokinetic Poisson and Ampere equations) are solved for the electrostatic potential and the parallel magnetic potential, respectively.

As part of the $\delta$-$f$ description, drift ordering with respect to the frequencies (diamagnetic frequency slower than ion gyrofrequency) and the fluctuation scales (parallel wavelength much longer than perpendicular) is assumed. The background parameters for electron and ion temperature assume isotropy (equal parallel and perpendicular kinetic energies) but the dynamics is not assumed to be isotropic. The salient parameters describing the dynamics are the local rho-star ($\rho_s/a$), beta ($\beta_e=\mu_o p_e/B^2$), and collisionality ($\nu_e a/c_s$). These are determined in an experiment by the density, temperature, and magnetic field. The local normalized parameters, which control the dynamics through their determination of how currents respond to fluctuations in the electron density and temperature and the electrostatic potential, are the drift-Alfvén inductivity $[\hat{\beta}=\beta_e(qR/L_\perp)^2]$, the electron inertia $[\hat{\mu}=(m_e/M_i)(qR/L_\perp)^2]$, and the drift-wave collisionality $[C=0.51(\nu_e L_\perp/c_s)\hat{\mu}]$. Here $\rho_s$ is the ion inertia drift scale, $c_s$ is the electron isothermal sound speed, and $L_\perp$ is the local profile scale length. For evaluation of situations with different gradients for density and ion and electron temperature, see the discussion in Ref. 17.

A brief review of the edge situation and the translation of experimental parameters into these quantities is given in Ref. 17. For GEMR the dimensionless inputs are $\beta_e$ and $\rho_s/a$ and $\nu_e(a/c_s)$ and the initial profiles for the density and the ion and electron temperatures and the magnetic pitch parameter $q$. The GEM model does *not* make assumptions about collisionality, but uses a treatment that is suitable for both collisionless and collisional regimes for all dissipative processes. The main limitation here is that there is no model for trapped particles. In the strongly collisional regime of the C-Mod edge, the forms of the dissipation processes reduce to those represented by the Braginskii equations.[18]

There are no neutrals in the GEMR model. The target density and temperature profiles are maintained by artificial sources of particles and heat inside the last closed flux surface. Since the profiles are treated self-consistently, the perpendicular flows evolve via charge separation, E×B compression, and parallel balance responses. Small changes in the zonal component of the pressure lead to geodesic acoustic energy transfer and several concurrent damping mechanisms maintain the general force balance.[18,19]

### B. Computational setup

The GEMR computations were 3D within the 2D axisymmetric geometry and covered the entire poloidal and toroidal domains of the flux surface. The flux surface geometry was circular with a Shafranov shift self-consistent to the dynamically varying pressure gradient.[2] The angle coordinates are a field-aligned form of the Hamada angles.[14] The computational grid was 64 radial, 1024 in the perpendicular angle, and 16 along the field line over one poloidal connection length (this translates to roughly 1024 times $q$ or about 2700 points along the poloidal angle in the poloidal plane). The limiter was described by a Debye sheath cut at $+/-\pi$ in the poloidal angle for $r/a>1.0$. Due to the coordinate transformation the sheath enters the parallel dimension only; details of the implementation appear in Ref. 19.

GEMR is a local model intended to simulate the turbulence in a single radial region in the C-Mod SOL. However, an edge region at $r/a<1$ was also included within the model to locate the boundary source away from the SOL region of interest. Therefore, the radial domain in the model was set up to be $0.94<r/a<1.06$, but only the results of the model within its SOL region at $1.012<r/a<1.042$ were used to compare with the GPI experimental data. The model heat and particles sources at $0.94<r/a<0.95$ were adjusted such that the resulting gradient at $r/a\sim1.0$ in the model approximately matched the gradient at the experimental region of interest ($\rho\sim1.3$ cm). Thus the GEMR model does *not* attempt to simulate the actual radial profile of the edge or SOL of C-Mod, but rather attempts to simulate the turbulence in a single radial region of the SOL in a self-consistent manner. The model is not realistic enough to compare its heat and particle fluxes with the actual heat and particle fluxes in the C-Mod SOL.

The radial boundary conditions on all 14 variables (12 dependent variables and both fields) were Neumann (zero radial partial derivative) on the inside and Dirichlet (zero value) on the outside. Source and sink control of these was done with levels chosen to maintain the values for SOL input plasma parameters from C-Mod, using the methods detailed in Sec. IV of Ref. 20. The resulting turbulence in the entire radial range of the model was first controlled to be saturated (using every energetic time trace, with the parallel kinetic energy taking the longest to saturate) and then computational diagnostics were taken at $1.012<r/a<1.042$ for $200<c_st/a<400$. This diagnostic information is then used to evaluate the comparisons to the experimental data taken with the GPI diagnostic.

The radial size of the GEMR simulation domain was fixed at ~2.6 cm for all cases, so each of the 64 radial grid points had a radial size of $\sim2\rho_s$. This limits the spectral range to $k_r\rho_s\leq1-2$, with the spectral resolution scaling as $1/B$. However, this range was easily sufficient to obtain converged cases, as discussed in Sec. IV D. From the theoretical perspective, it is believed that ion gyroradius scale effects are negligible in the SOL [e.g., Ref. 12]. Note that the $k$-resolution in this GEMR gyrofluid simulation is greater than that for any 3D Braginskii fluid simulation.

TABLE II. GEMR SOL model parameters for the computations.

| $B_o$ (T) | $n$ ($/10^{13}$ cm$^{-3}$) | $T$ (eV) | $C$ | $\hat{\mu}$ | $\hat{\beta}$ |
|---|---|---|---|---|---|
| 2.7 | 1.6 (low) | 15 | 13 | 2 | 0.05 |
| 2.7 | 3.6 (high) | 19 | 18 | 2 | 0.14 |
| 3.8 | 2.2 (low) | 22 | 8 | 2 | 0.05 |
| 3.8 | 4.6 (high) | 25 | 13 | 2 | 0.12 |
| 5.4 | 1.8 (low) | 16 | 12 | 2 | 0.02 |
| 5.4 | 3.2 (high) | 19 | 16 | 2 | 0.03 |

### C. C-Mod cases

Six different runs of GEMR were made as shown in Table II, corresponding to low and high density cases for each of the three $B$ fields used in this experiment. All cases assumed $R_o=67$ cm, $a=21.6$ cm, $q(r)=2.7(r/a)^2$, $\kappa=1$, $Z_{\text{eff}}=2$, $M_i=2$, $M_i/m_e=3670$, and $T_i=T_e$ in the background parameters.

The dimensionless parameters $\hat{\beta}$, $\hat{\mu}$, and C shown in Table II (see Ref. 17 for definitions) are typical values for these cases based on the $n$ and $T_e$ and on a perpendicular pressure scale length of $L_\perp\sim2$ cm (which is typical for the SOL in these cases). The collisionality C was relatively high in all cases, as usual in the C-Mod edge, which should justify the neglect of trapped electrons in the GEMR model (however, see the commentary given in Sec. V B). The parameter $\hat{\mu}=2$ in cases and the normalized $\hat{\beta}$ is $\ll1$ in all cases, indicating dominantly resistive behavior in the electron responses.

### D. Analysis of GEMR outputs

For comparison with the GPI data, the 2D density and temperature outputs from GEMR were converted into $D_\alpha$ light emission using the approximation[16] $D_\alpha\sim n^\alpha T_e^\beta$, where $\alpha$ and $\beta$ were calculated from tables of the atomic physics of $D_\alpha$ emission using the measured SOL values of $n$ and $T_e$ listed in Table II. For these cases $\alpha\sim0.4-0.6$ and $\beta\sim0.6-0.8$. There was a very high correlation between the local density and electron temperature fluctuations in the GEMR outputs ($\geq0.95$), thus the spectra and cross-correlations of the $D_\alpha$ light signals were the same as those for the $n$ and $T_e$ signals themselves, independent of $\alpha$ and $\beta$. However, the relative fluctuation level in $D_\alpha$ should vary linearly with $(\alpha+\beta)$ so is not simply the same as $\tilde{n}/n$.

The $D_\alpha$ emission outputs from the GEMR runs were then smoothed to match instrumental resolution of the GPI geometry and views, as described in Secs. II B and II C. The influence of this space and time smoothing on the GEMR results is illustrated in Table III, which shows turbulence results for one case (3.8 T high density). The "none" column in Table III has no smoothing, the "diode" column has smoothing over the ~0.3 cm radial and ~0.3 cm poloidal width of the detector view and the time response of the diodes (~2.5 $\mu$s), and the "total" column adds an additional ~0.8 cm poloidal smoothing due to the viewing angle of the GPI with respect to $B$, which significantly increased the po-

TABLE III. Smoothing of GEMR (3.8 T high $n$ case).

| Parameter | None | Diode | Total |
|---|---|---|---|
| $L_{pol}$ (cm) | 0.70 | 0.94 | 1.25 |
| $L_{rad}$ (cm) | 0.47 | 0.63 | 0.66 |
| $\tau_{auto}$ ($\mu$s) | 9.6 | 12.1 | 12.6 |
| $\delta D_\alpha / D_\alpha$ (%) | 9 | 8 | 7 |
| $V_{pol}$ (km/s) | 0.90 | 1.0 | 1.6 |
| $V_{rad}$ (km/s) | 0.67 | 0.79 | 0.64 |

loidal correlation length and velocity. The "total" was the smoothing level used for comparisons with the GPI data in Sec. IV.

The calculated GEMR turbulence properties were then averaged over ±3 cm in the poloidal direction (i.e., pixels 10–250), ~0.6 cm in the radial direction (i.e., pixels 39–55 corresponding to SOL region at $1.012 < r/a < 1.042$), and 1.4 ms in time (i.e., 4000 time snapshots). The turbulence properties were nearly constant in the model over this space and time range.

## IV. COMPARISONS BETWEEN GPI AND GEMR

In this section the GEMR model results are compared with the GPI turbulence measurements. The GPI results were averaged over the radial and poloidal arrays shown in Fig. 3, as discussed in Sec. II. The GEMR code output was smoothed to simulate the GPI instrumental resolution, as discussed in Sec. III. The variation of the turbulence characteristics with $B$ and $\langle n \rangle$ are described in Secs. IV A–IV C and comparisons of the frequency and $k_{pol}$ spectra are described in Sec. IV D.

### A. Correlation lengths

Figure 5 shows a comparison of the poloidal and radial correlation lengths $L_{pol}$ and $L_{rad}$ as a function of $B$ for the GPI results and the GEMR model. For this analysis the local correlations length $L_{pol}$ (or $L_{rad}$) were defined the same way for both the GPI and the GEMR results, namely, $L = 1.66(\delta x)/(-\ln C_{12})^{1/2}$, where $C_{12}$ is the zero-time-delay cross correlation coefficient between two nearby poloidally or radially points separated by $\delta x$. This estimate assumes that the correlation function is a Gaussian of width $L$ (FWHM) and gives the size scale of the turbulence in these directions averaged over the whole $(\omega, k)$ spectrum. The results are roughly independent of $\delta x$ in this data and the $L$ values obtained using these two-point correlations are consistent with the correlation lengths obtained using a Gaussian fit of the correlation functions obtained from the five points in each array.

For Fig. 5 the GPI data points were averaged over the four pairs of adjacent points in the radial array (Fig. 3), over 10 ms at the peak of the GPI gas puff (i.e., 1.00–1.01 s), and over all shots at a given $B$ (Table I). The error bars on the GPI data are the standard deviation of the shot-to-shot variations. For the GEMR results, the averaging was done over the radial and poloidal ranges described in Sec. III D. The GEMR results for the low density and high density points versus $B$ are connected together by straight lines.

Figure 5(a) shows that the poloidal correlation lengths for the GPI and GEMR results are similar to each other to within ~20% at each $B$. The GPI results for $L_{pol}$ are roughly independent of $B$ (to within the error bars), while the GEMR results decrease by ~10%–20% with $B$. Note that the GEMR poloidal correlation lengths were significantly increased by the poloidal smoothing, as shown in Table III. Figure 5(b) shows that the radial correlation lengths in the GPI results were ~1.5–2 times larger than the GEMR re-

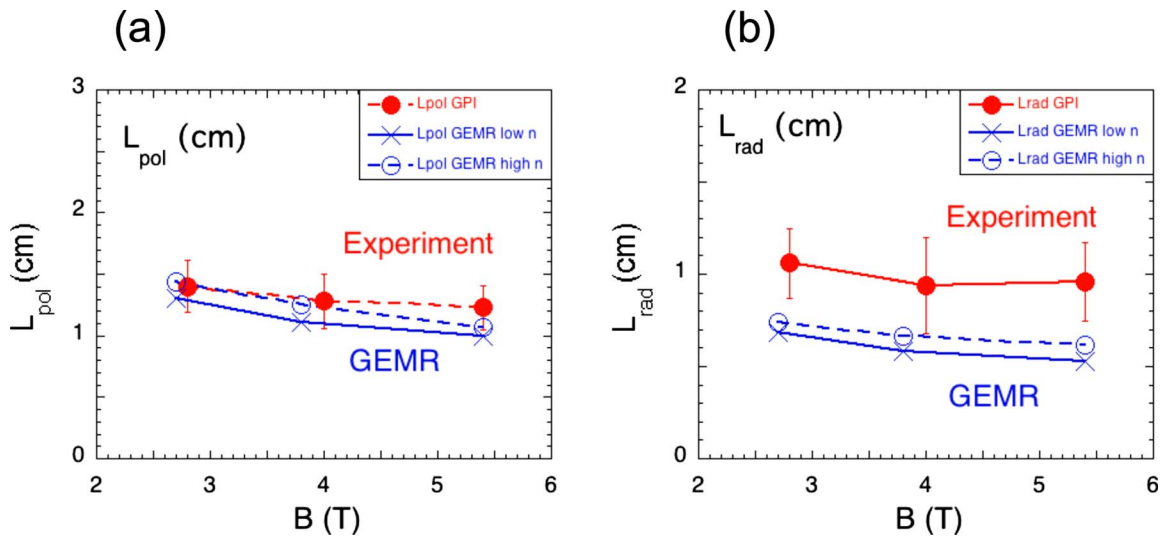


FIG. 5. (Color online) Comparison of the turbulence correlation lengths vs $B$ in the (a) poloidal and (b) radial directions. The GPI results are averaged over the radial detector locations in Fig. 3 and over all discharges at a given $B$ and the error bars are standard deviations. The GEMR results are averaged over the radial and poloidal ranges and smoothed to match the instrumental resolution, as described in Sec. III D. The poloidal correlation lengths of GPI and GEMR are within 20% of each other for all $B$, while the radial correlation length of the GPI results are ~1.5–2 times larger than those from GEMR.

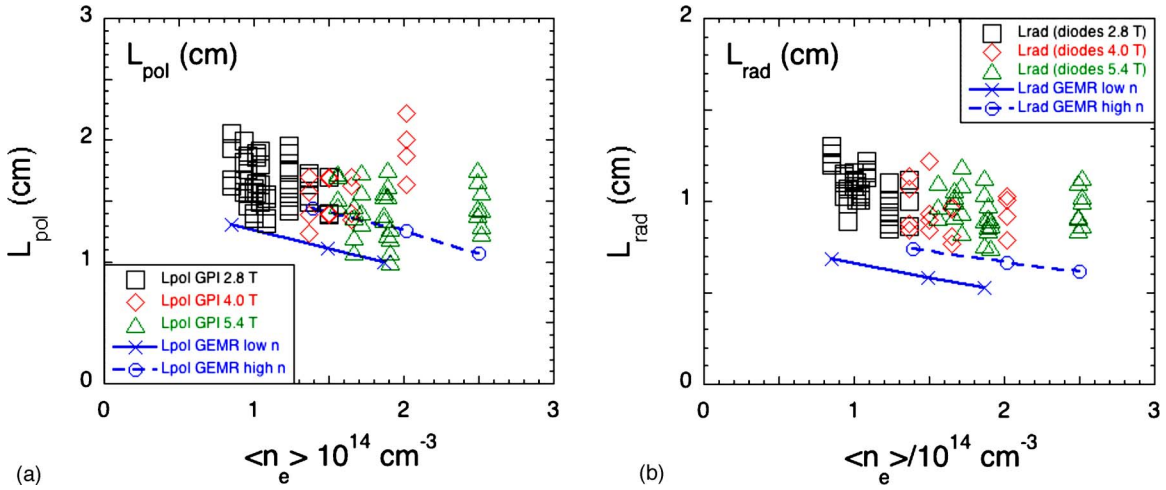


FIG. 6. (Color online) Comparison of the turbulence correlation lengths vs $\langle n_e \rangle$ in the (a) poloidal and (b) radial directions. The GPI data are shown for each discharge and each radial detector location in this experiment. The GPI results are color-coded according to $B$ and the GEMR results are for the same cases as Fig. 5. There is a slight decrease in the correlation lengths with increasing density in both the GPI data and GEMR results.

sults. Again, the GPI results are roughly independent of $B$, while the GEMR results decreased by ~10%–20% with $B$. Therefore these SOL correlation lengths do not simply scale with $\rho_s$, as discussed in Sec. V A. Both the GPI and GEMR results have the poloidal correlation lengths ~1.5–2 times larger than the radial correlation lengths.

In Fig. 6 the individual GPI correlation lengths $L_{\mathrm{pol}}$ in (a) and $L_{\mathrm{rad}}$ in (b) are shown for each pair of points and for each shot as a function of the line-averaged density $\langle n_e \rangle$ and color coded according to $B$. There was a slight (~10%–20%) decrease in the GPI correlation lengths with increasing density and also a slight decrease in GEMR correlation lengths with increasing density. Note that there was a correlation between $B$ and $\langle n_e \rangle$ in the experimental data, so a causal connection between $\langle n_e \rangle$ and these correlation lengths cannot be directly inferred.

### B. Autocorrelation times and propagation speeds

Figure 7 shows the autocorrelation times $\tau_{\mathrm{auto}}$ for the same GPI data and GEMR cases discussed in Sec. IV A. Here $\tau_{\mathrm{auto}}$ is defined as the time over which the autocorrelation function at a fixed point reaches 0.5. The GPI results of Fig. 7(a) are averaged over the five views in the radial array and over all shots at each $B$. The GEMR results were averaged as in Figs. 5 and 6. The GPI results of Fig. 7(b) are shown for each point in the radial array and each shot and color coded according to $B$ as in Fig. 6.

Figure 7(a) shows that the average $\tau_{\mathrm{auto}}$ in the GPI data was ~16 $\mu$s at $B_o$=2.8 T and ~34 $\mu$s at $B_o$=5.4 T, i.e., had a factor of 2 increase over this range of $B$. The $\tau_{\mathrm{auto}}$ from the GEMR simulations was $\sim 10 \pm 2$ $\mu$s over this range of $B$, with perhaps a slight decrease with $B$. Thus there was a

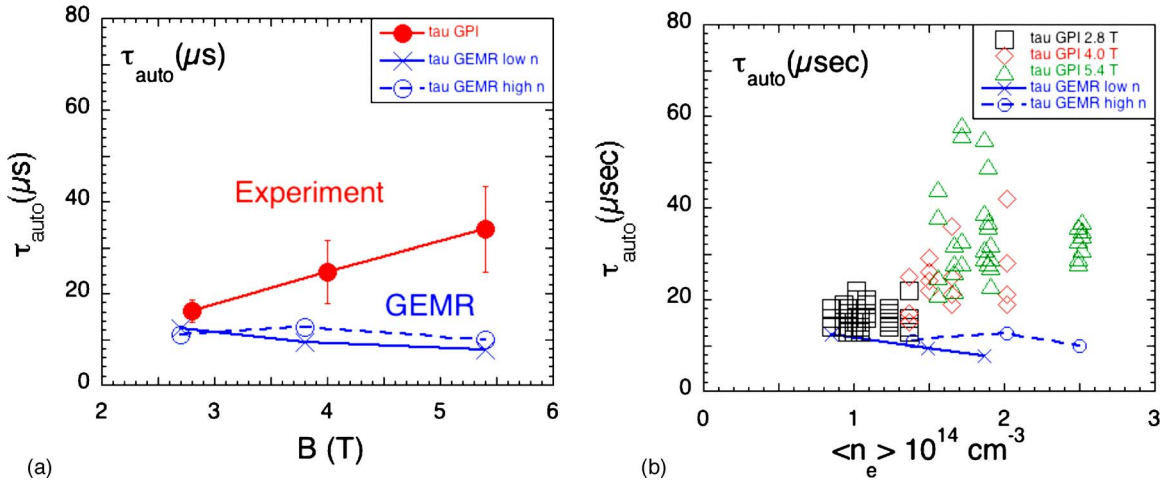


FIG. 7. (Color online) Comparison of the turbulence autocorrelation times for the GPI data and GEMR results as a function of (a) the magnetic field $B$ and (b) the line-averaged plasma density. For (a) the results are averaged as in Fig. 5, while for (b) the individual results are presented as in Fig. 6. The GPI correlation times increase significantly with $B$, while the GEMR results do not. For (b) the GPI data are shown as a function of the line-averaged density for each shot and each radial location, and color code according to $B$. There is little or no density variation in the measured autocorrelation times at a fixed $B$.

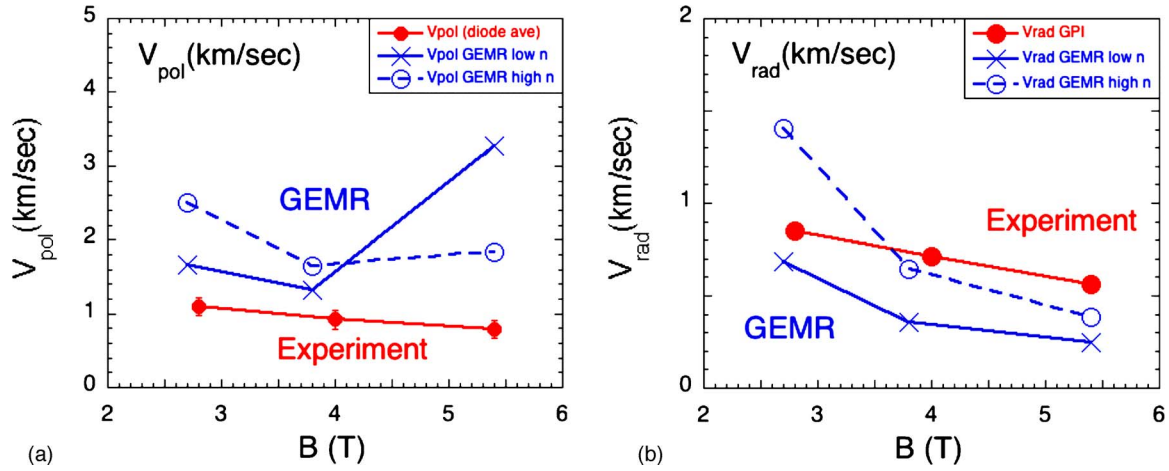


FIG. 8. (Color online) Comparison of the turbulence propagation velocity in the (a) radial and (b) poloidal directions for the GPI data and the GEMR results. The results are averaged as for Fig. 5. The poloidal propagation in (a) is ~1 km/s in the GPI data and ~1–3 km/s in the GEMR results, both in the ion diamagnetic drift direction. The radial propagation in (b) is outward at ~0.5–1 km/s for both the GPI results and the GEMR results.

significant difference between GPI and GEMR in the scaling of $\tau_{auto}$ with $B$. Figure 7(b) shows that $\tau_{auto}$ increased with the line-averaged density $\langle n_e \rangle$, but again that this may be associated with the codependency of $\langle n_e \rangle$ and $B$ in this database.

Figure 8 shows the propagation speeds of the turbulence in the GPI and GEMR results for both the poloidal and radial directions. These speeds were determined from the average time delay in the peaks of the cross-correlation function, as used in Sec. IV A. The poloidal speeds in Fig. 8(a) were ~1 km/s in the GPI data, with a slight trend to lower speeds at higher $B$, and ~1–3 km/sec in the GEMR results, both in the ion diamagnetic drift direction. For the radial propagation speeds in Fig. 8(b) both the GPI results and the GEMR results showed an outward radial propagation speed of ~0.5–1.5 km/s and both had a decrease in this speed with increasing $B$. This radial speed is consistent with the radial propagation of "blobs" as measured in the SOL of C-Mod in other experiments.[21] It should be noted that for tilted 2D structures the propagation velocity in one direction can project into an apparent propagation velocity in the orthogonal direction. Therefore the results of Fig. 8 should be interpreted as a comparison between the experiment and code results and not as an unambiguous measurement of the radial or poloidal turbulence velocities.

### C. Fluctuation levels and statistical moments

Figure 9 shows the relative fluctuation levels $\delta D_\alpha / D_\alpha$ for the same GPI and GEMR results as described in Secs. IV A and IV B. Figure 9(a) shows that the GPI fluctuation levels were ~3–10 times lower in the GEMR results than in the GPI data. There was also a trend in the GEMR results toward lower fluctuation levels at higher $B$, which was not consistently present in the GPI data. Figure 9(b) shows the same relative fluctuation level for each radius and shot, color coded according to $B$. There is a trend in both the GEMR and GPI results toward lower fluctuation levels with higher $\langle n_e \rangle$ at each $B$ field.

Figure 10 shows the calculated skewness and kurtosis

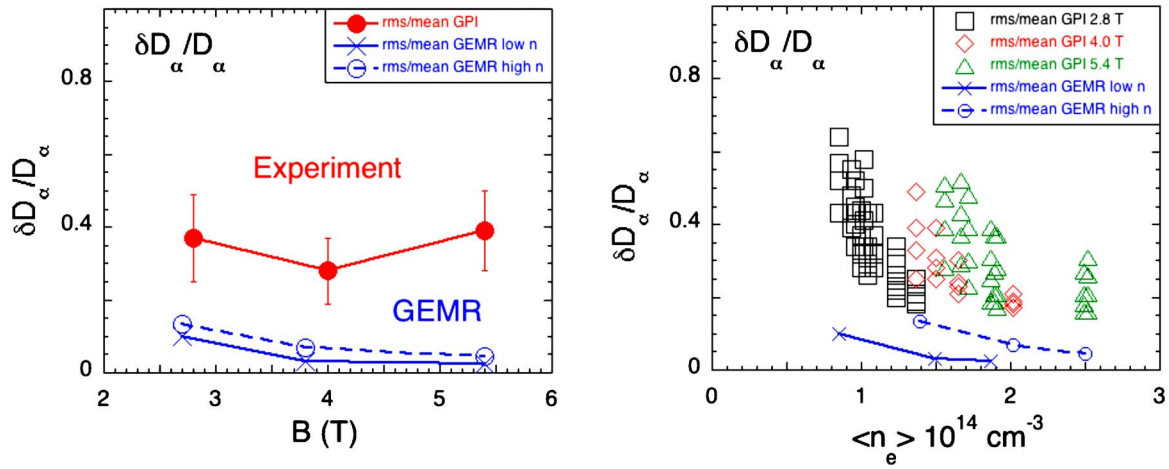


FIG. 9. (Color online) Comparison of the relative $D_\alpha$ fluctuation levels for the GPI and GEMR results as a function of (a) $B$ and (b) $\langle n_e \rangle$. For (a) the results are averaged as in Fig. 5, while for (b) the individual results are presented as in Fig. 6. The GEMR results show a fluctuation level three to ten times lower than the GPI data. Both the GPI data and GEMR results show a trend toward lower fluctuation levels at higher density.

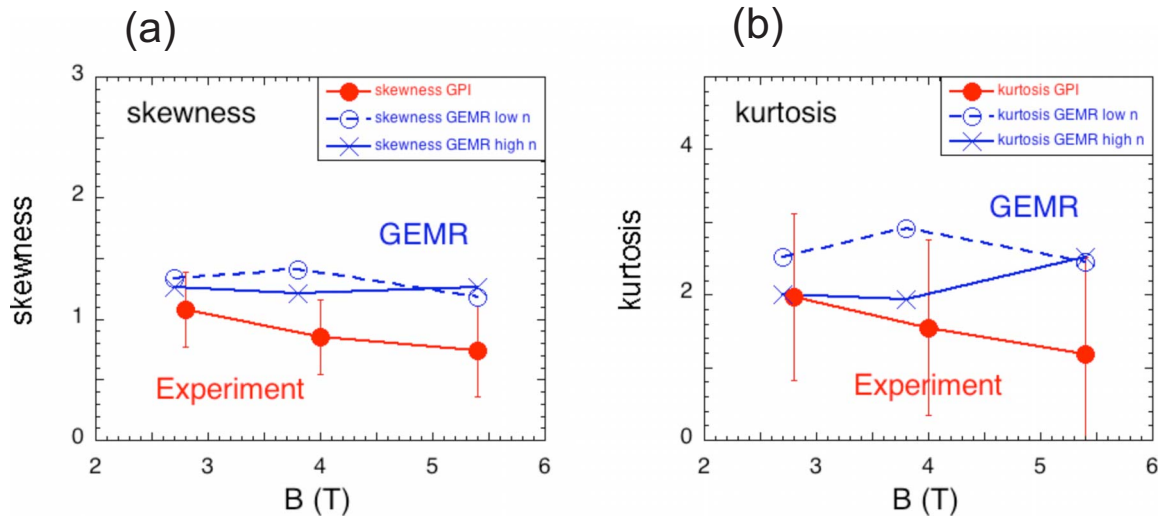


FIG. 10. (Color online) Comparison of the skewness and kurtosis for the GPI and GEMR results for the same cases as in Fig. 9. The skewness and kurtosis are positive for both the GPI and GEMR results, which is generally consistent with the presence of intermittency or "blobs," as in other experiments and simulations.

for the GEMR and GPI results as a function of $B$ for the same data set. Both the GPI and GEMR results showed a positive skewness ~1 and kurtosis ~2. This positive skewness and kurtosis are similar to other SOL measurements and models and associated with intermittency or blobs.[3,15] There was also a slight trend for decreasing $S$ and $K$ with increasing line-averaged density (not shown).

### D. Frequency and $k_{pol}$-spectra

Figure 11 shows the fluctuation power spectra versus frequency for the GPI and GEMR results for the high density cases at $B_o$=2.8 T and $B_o$=5.4 T (similar comparisons are obtained for all other cases). These spectra are averaged over the same radial range of GPI points and GEMR results as for Secs. IV A–IV C. The amplitudes of the GPI and GEMR spectra at each $B$ are normalized to each other where shown. The finite sample length of the GEMR analysis limits its spectrum to frequencies above ≥0.5 kHz and the time smoothing of the GEMR results significantly attenuates its spectrum above ~400 kHz. For these (and all other) cases the shapes of the frequency spectra from GEMR are at least qualitatively similar to those from the GPI over the range ~0.5–100 kHz. For the high $B$ case there is relatively more spectral power in the GPI signals at lower frequency ($f$~1 kHz), which makes the autocorrelation time longer at higher $B$. Note that the apparent steps in the GEMR frequency spectra (e.g., at ~10 kHz in the 5.4 T case) are not a consistent features of these GEMR results.

Figure 12 shows the poloidal $k$-spectra evaluated for the same two cases as in Fig. 11, i.e., $B_o$=2.8 T and 5.4 T. These $k$-spectra were evaluated in the same way for both the GEMR and the GPI results with the method of Beall *et al.*[22]

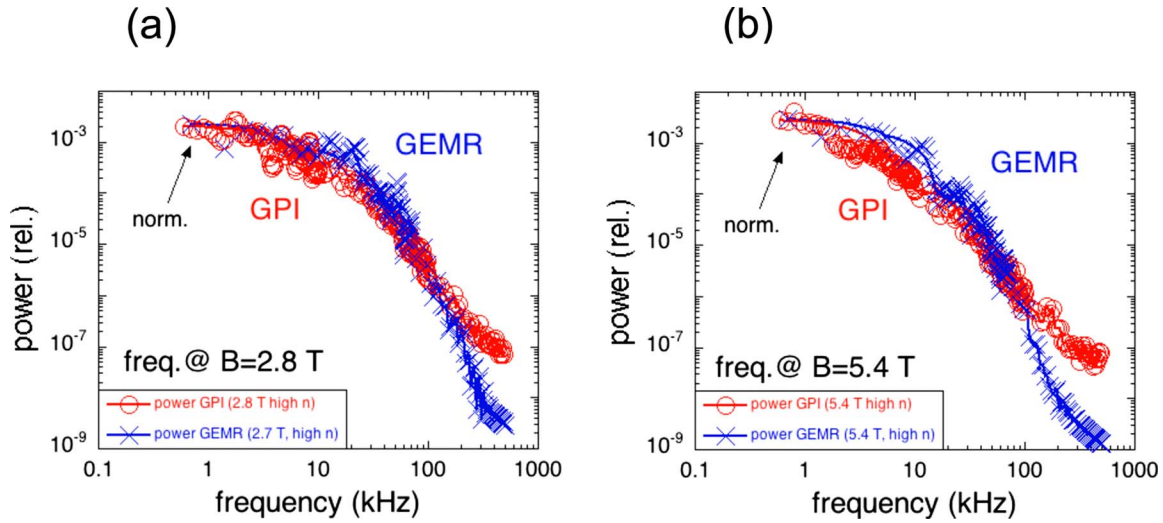


FIG. 11. (Color online) Comparison of the frequency spectra of the GPI and GEMR results for the (a) $B_o$=2.8 T and (b) 5.4 T (high density) cases in this experiment. These spectra are averaged over the GPI radial array and the GEMR region described in Sec. III D and are normalized to each other where shown. The shapes of the spectra from GEMR are similar to those from GPI over the range ~0.5–100 kHz in all cases.

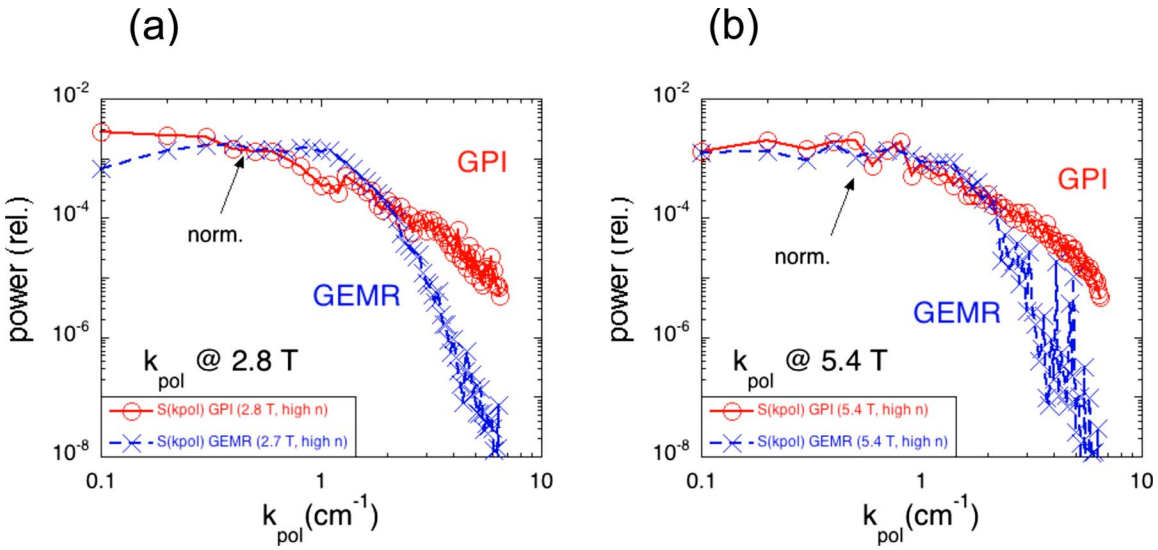


FIG. 12. (Color online) Comparison of the poloidal $k$-spectra of the GPI and GEMR results for the (a) $B_o$=2.8 T and (b) 5.4 T cases. These spectra are averaged over the GPI radial array and the GEMR region described in Sec. III D and are normalized to each other where shown. The shapes of all these $k_{\mathrm{pol}}$ spectra are similar for to each other for $k \leq 1$ cm$^{-1}$. The GEMR spectra fall off rapidly for $k \geq 2$ cm$^{-1}$ due to the poloidal smoothing.

using the same pairs of points as for the poloidal correlation and velocity measurements (the GEMR spectra obtained in this way were similar to the spectra obtained from a direct FFT of the GEMR poloidal grid of 256 points). The GPI and GEMR $k_{\mathrm{pol}}$-spectra are shown only for the dominant sign of $k_{\mathrm{pol}}$ (in the direction of propagation) and the amplitudes were normalized to each other where shown. The GPI spectra are at least qualitatively similar to the GEMR spectra at $k_{\mathrm{pol}} < 1$ cm$^{-1}$, but with somewhat more power at low $k$ in the GPI data than in the GEMR spectrum for the 2.8 T case. For $k_{\mathrm{pol}} > 2$ cm$^{-1}$ the GEMR spectra fall below the GPI spectra mainly due to the poloidal smoothing correction.

For these SOL conditions the dominant part of the measured spectrum at $k \leq 1$ cm$^{-1}$ corresponds to $k_{\mathrm{pol}}\rho_s \leq 0.02$ at $B_o$=2.8 T and $k_{\mathrm{pol}}\rho_s \leq 0.01$ at $B_o$=5.4 T, as noted previously in C-Mod.[15] Thus both the measured and modeled $k$-spectra fall in the range $k_{\mathrm{pol}}\rho_s \ll 1$, as is usual for SOL turbulence measurements.[3] Note that the *unsmoothed* $k_{\mathrm{pol}}$ power spectra from GEMR typically decreases like $k^{-2-3}$ above $k \sim 1$ cm$^{-1}$, so that the GEMR $k$-spectral resolution of $k_{\mathrm{pol}}\rho_s \leq 1-2$ was easily sufficient to obtain converged cases.

## V. DISCUSSION

This paper described comparisons of SOL turbulence measurements in Alcator C-Mod with the GEMR model, which is a 3D first-principles turbulence computation done under broadband electromagnetic conditions. In general, there was good qualitative agreement between the experimental results and the GEMR model and a variable degree of quantitative agreement depending on the specific type of comparison. In Sec. V A these comparisons are summarized, in Sec. V B their limitations and uncertainties are discussed, in Sec. V C some directions for improvement are suggested, and Sec. V D contains the conclusions.

### A. Summary of experiment versus GEMR comparisons

In Sec. IV the following comparisons between experiment and the GEMR model were made: poloidal and radial correlation lengths (Figs. 5 and 6), autocorrelation times (Fig. 7), poloidal and radial turbulence velocities (Fig. 8), relative $D_\alpha$ fluctuation levels and statistical moments (Figs. 9 and 10), frequency spectra (Fig. 11), and poloidal $k$-spectra (Fig. 12). The same analysis tools were used for both experimental and model results.

The closest agreement between experiment and model was found for the poloidal correlation lengths, which agreed to within ~20%, while the radial correlation lengths agreed to within a factor of ~1.5–2. The poloidal and radial correlation lengths in both the experiment and model varied by <20% over a ×2 range in $B$, as shown in Fig. 5. Thus the correlation lengths do not necessarily scale with $\rho_s$, as would be expected for a drift-wave type scaling associated with the effective adiabatic response on closed field lines. In the SOL the field lines are open in the parallel direction and the turbulence can have flutelike magnetohydrodynamic (MHD) behavior, which does not scale simply with $\rho_s$. Other points of reasonably good agreement between experiment and model were the radial turbulence velocity [Fig. 8(b)], the higher order statistical moments (Fig. 10), and the frequency and $k_{\mathrm{pol}}$ spectra (Fig. 11).

The least satisfactory agreement between experiment and modeling was in the relative $D_\alpha$ fluctuation levels, which were three to ten times higher in the experiment than in the modeling. However, this is also the quantity which varied the most with radius in the experiment (see Fig. 4), so the comparison was not expected to be precise. Another point of disagreement was in the $B$ scaling of the autocorrelation

time, which increased by two times with increasing $B$ in the experiment, but slightly decreased with $B$ in the modeling (Fig. 7).

### B. Limitations and uncertainties

A general limitation of these experiments was that they covered a relatively small range of $B$, $\langle n_e \rangle$, and SOL parameters, as summarized in Tables I and II. The SOL collisionality was always relatively high and the SOL beta was always relatively low, which gave a limited test of the model scaling. In addition, only near-circular, inner-wall limited plasmas were used in this experiment in order to match the GEMR geometry.

There were some diagnostic limitations as well. These GPI measurements were made only for the middle-to-outer region of the SOL, so did not include the "near-SOL" just outside the last closed flux surface, which may have different characteristics.[23] Also, the GPI sightlines for this experiment were oriented toroidally and not along the local magnetic field, which introduced a significant loss of poloidal resolution (Table III). This was corrected by smoothing the GEMR results, but the degree of smoothing was based on modeling by DEGAS-2 and not directly measured, and so was therefore somewhat uncertain.

A general limitation of these results is that the GPI data were only available for one dimensional (1D) arrays for two different directions (radial and poloidal), rather than in the full 2D plane; thus the local direction and shape of these turbulent structures in the radial versus poloidal plane was not determined. One symptom of this limitation is the relatively large range of the ratios $\tau_{\mathrm{auto}}/(L_{\mathrm{pol}}/V_{\mathrm{pol}}) \sim 1.5-2.5$ and $\tau_{\mathrm{auto}}/(L_{\mathrm{rad}}/V_{\mathrm{rad}}) \sim 0.5-2$, instead of $\tau_{\mathrm{auto}}/(L/V) \sim \mathrm{const}$ as would be the case for turbulence moving in a known 1D direction. Nevertheless, the 1D comparisons of experimental data with the model should still be valid even with this limitation. Another geometrical limitation was that the poloidal correlation lengths and velocities were measured for only one radial location and not for the whole radial range of the data used for evaluating the correlation times and fluctuation levels, so that any radial variation in the $L_{\mathrm{pol}}$ or $V_{\mathrm{pol}}$ (such as shown for $L_{\mathrm{rad}}$ and $\tau_{\mathrm{auto}}$ in Fig. 4) could not be measured. These limitations can be overcome in the future by using a 2D photodiode array or an ultrafast 2D imaging system.

A basic limitation of GEMR is that it is a local model for the turbulence in a single radial region and so does not attempt to self-consistently calculate the radial profile of the turbulence in the experiment. The inputs to GEMR came from a single point in the middle of the SOL and so the model only approximately simulated the SOL parameters over the radial range of the turbulence measurements. However, since the turbulence properties were approximately constant over the radial range of these measurements (Fig. 4), this comparison is reasonably appropriate.

In terms of the physics modeled, GEMR does not incorporate the possible effects of a large, isolated density perturbation (blob) originating in one radial region and then carrying energy to another region with strongly different local parameters, and it also does not calculate the SOL width from first principles. Due to the $\delta$-$f$ ordering, any attempt to compute both the edge [last scale length before the last closed flux surface (LCFS)] and the SOL is predetermined to calculate the gradients in one of these regions incorrectly. Concurrent with this is the implicit assumption of small fluctuation level. While an $L$-mode edge with $\sim 20\%$ fluctuations can be captured, a SOL dominated by localized structures with an effective fluctuation level near $\sim 100\%$ cannot.

One further limitation is the neglect of trapped particle effects. While we may expect these not to enter due to the large collisionality, we do note that in a model with strong parallel dynamics the current fluctuations are carried down the field lines by waves, and the character of this depends strongly on perpendicular scale. At larger scale the parallel coupling of Alfvén transients to the pressure is much less strongly resistive and depends on the reactive forces part of the dynamics. In a situation where the magnetic topology by itself would indicate over 80% of the particles are poloidally trapped (even in the SOL), the size of the coupling coefficients acting directly between the part of phase space responsible for the parallel currents and the inductive and static parts of the parallel electric field are different than they are in a pure fluid model. This is one possible cause of the inability of GEMR to capture the largest scales in the dynamics (by overestimating this "adiabatic coupling") and its lack of nonlocal blob dynamics would be another.

Models that may be able to treat these effects are under construction, but at the present time they are not close to availability for a study such as this one. For example, fully nonlinear gyrokinetic models are eventually needed, but the computational resources available to the present study, while significant, would not have been remotely adequate for gyrokinetic computation under the same conditions (an increase of roughly two orders of magnitude would be required to reproduce the same level of spatial resolution and temporal scale).

### C. Directions for improvement

These comparisons of GEMR computations with C-Mod SOL turbulence could be extended to include the 2D structure and motion of the turbulence, e.g., for intermittent blobs.[15] Further comparisons could also be made of the potential fluctuations and the $q(a)$ scaling. It would be useful to increase the range of SOL parameters, e.g., collisionality, beta, but experimentally this is not easily accomplished in C-Mod.

The framework for computation of SOL turbulence can be improved by incorporating magnetic divertor geometry, nonlocal models, and/or kinetic effects, which are beyond the scope of the present investigations. Use of the FEFI nonlocal gyrokinetic model is planned,[24] but a sheath model compatible with violent shear Alfvén dynamics in front of the divertor plate remains to be found. Various field-aligning methods for flux coordinates in the vicinity of the $X$-point are being developed and discussed, since previous ones (e.g., Refs. 2 and 25) are not adequate as they merely patch an edge onto a SOL.

### D. Conclusions

In conclusion, the GEMR turbulence model was at least partially successful in explaining the properties of the SOL turbulence in C-Mod over the range of $B_o = 2.7-5.4$ T in this experiment. The radial and poloidal correlation lengths and velocities were reproduced by the model to within about a factor of 2 and the frequency and $k_{pol}$ spectra had similar broadband shapes in the experiment and the model. The correlation lengths in both experiment and model only weakly decreased with $B$ and the $k_{pol}$ spectral power was dominantly located at $k\rho_s \ll 1$.

In general, the $B$ (i.e., $\rho_s$) scaling in turbulence theory results from effective adiabatic coupling between the potential and the electron pressure fluctuations, which enforce a "drift wave" or gyro-Bohm scaling. In the absence of this coupling the turbulence is hydrodynamic or MHD "flute-like." The main difference between SOL and edge turbulence is that this the flute-mode component is allowed in the SOL.[26] Therefore weakness of the $B$ scaling in these results indicates the C-Mod SOL is dominantly flutelike and the drift-wave component is rather weak.

However, the GEMR model significantly underestimated the relative fluctuation levels and the autocorrelation times at higher $B$ in this experiment. The model was also incomplete in that it did not attempt to explain either the radial profile of the SOL turbulence or the SOL transport, and the experimental data were incomplete in that it used only 1D radial and poloidal arrays and not the full 2D structure and motion of the SOL turbulence. A complete SOL turbulence model would also include magnetic divertor geometry and nonlocal and/or kinetic effects, which are beyond the scope of the present investigations.

### ACKNOWLEDGMENTS

We thank Olaf Grulke, T. S. Hahm, and Uli Stroth for helpful discussions. We also thank Steve Scott, Chuck Kessel, and Randy Wilson of PPPL and the C-Mod team for their support for this work, which was funded by U.S. DOE Contract No. DE-AC02-76CH03073 (PPPL) and USDOE Cooperative Agreement No. DE-FC02-99ER54512 (MIT). We thank the DEISA Consortium (www.deisa.org) and the Leibniz Rechenzentrum (TU Muenchen, Germany) for support of these computations as part of the DEISA/DECI project GEM in 2008.

[1] S. Scott, A. Bader, M. Bakhtiari, N. Basse, W. Beck, T. Biewer, S. Bernabei, P. Bonoli, B. Bose, R. Bravenec, I. Bespamyatnov, R. Childs, I. Cziegler, R. Doerner, E. Edlund, D. Ernst, A. Fasoli, M. Ferrara, C. Fiore, T. Fredian, A. Graf, T. Graves, R. Granetz, N. Greenough, M. Greenwald, M. Grimes, O. Grulke, D. Gwinn, R. Harvey, S. Harrison, T. C. Hender, J. Hosea, D. F. Howell, A. E. Hubbard, J. W. Hughes, I. Hutchinson, A. Ince-Cushman, J. Irby, T. Jernigan, D. Johnson, J. Ko, P. Koert, B. LaBombard, A. Kanojia, L. Lin, Y. Lin, B. Lipschultz, J. Liptac, A. Lynn, P. MacGibbon, E. Marmar, K. Marr, M. May, D. R. Mikkelsen, R. McDermott, A. Parisot, R. Parker, C. K. Phillips, P. Phillips, M. Porkolab, M. Reinke, J. Rice, W. Rowan, M. Sampsell, G. Schilling, A. Schmidt, N. Smick, A. Smirnov, J. Snipes, D. Stotler, J. Stillerman, V. Tang, D. Terry, J. Terry, M. Ulrickson, R. Vieira, G. Wallace, D. Whyte, J. R. Wilson, G. Wright, J. Wright, S. Wolfe, S. Wukitch, G. Wurden, H. Yuh, K. Zhurovich, J. Zaks, and S. Zweben, Nucl. Fusion **47**, S598 (2007).
[2] B. Scott, Contrib. Plasma Phys. **46**, 714 (2006).
[3] S. J. Zweben, J. A. Boedo, O. Grulke, C. Hidalgo, B. LaBombard, R. J. Maqueda, P. Scarin, and J. L. Terry, Plasma Phys. Controlled Fusion **49**, S1 (2007).
[4] O. E. Garcia, R. A. Pitts, J. Horacek, J. Madsen, V. Naulin, A. H. Nielsen, and J. J. Rasmussen, Plasma Phys. Controlled Fusion **49**, B47 (2007); W. Fundamenski, O. E. Garcia, V. Naulin, R. A. Pitts, A. H. Nielsen, J. J. Rasmussen, J. Horacek, J. P. Graves, and JET EFDA Contributors, Nucl. Fusion **47**, 417 (2007).
[5] R. H. Cohen, B. LaBombard, D. D. Ryutov, J. L. Terry, M. V. Umansky, and S. Zweben, Nucl. Fusion **47**, 612 (2007).
[6] D. A. D'Ippolito, J. Boedo, D. P. Lundberg, R. Maqueda, J. R. Myra, D. A. Russell, D. P. Stotler, and S. J. Zweben, in *Proceedings of the 22nd IAEA Fusion Energy Conference*, Geneva 2008 (IAEA, Vienna, 2009), Paper No. IAEA-CN-165/TH/P4-17.
[7] A. E. White, L. Schmitz, G. R. Mckee, C. Holland, W. A. Peebles, T. A. Carter, M. W. Shafer, M. E. Austin, K. H. Burrell, J. Candy, J. C. Deboo, E. J. Doyle, M. A. Makowski, R. Prater, T. L. Rhodes, G. M. Staebler, G. R. Tynan, R. E. Waltz, and G. Wang, Phys. Plasmas **15**, 056116 (2008).
[8] N. Mahdizadeh, F. Greiner, T. Happel, A. Kendl, M. Ramisch, B. D. Scott, and U. Stroth, Plasma Phys. Controlled Fusion **49**, 1005 (2007).
[9] B. Scott, Plasma Phys. Controlled Fusion **49**, S25 (2007).
[10] V. Naulin, J. Nucl. Mater. **363–365**, 24 (2007).
[11] S. Krasheninnikov, D. A. D'Ippolito, and J. R. Myra, J. Plasma Phys. **74**, 679 (2008).
[12] T. Rognlien, Plasma Phys. Controlled Fusion **47**, A283 (2005).
[13] B. Scott, Phys. Plasmas **12**, 102307 (2005).
[14] B. Scott, Phys. Plasmas **8**, 447 (2001).
[15] J. L. Terry, S. J. Zweben, K. Hallatschek, B. LaBombard, R. J. Maqueda, B. Bai, C. J. Boswell, M. Greenwald, D. Kopon, W. M. Nevins, C. S. Pitcher, B. N. Rogers, D. P. Stotler, and X. Q. Xu, Phys. Plasmas **10**, 1739 (2003).
[16] D. P. Stotler, J. Boedo, B. LeBlanc, R. J. Maqueda, and S. J. Zweben, J. Nucl. Mater. **363–365**, 686 (2007).
[17] B. Scott, Plasma Phys. Controlled Fusion **45**, A385 (2003).
[18] B. Scott, Phys. Plasmas **14**, 102318 (2007).
[19] T. Ribeiro and B. Scott, Plasma Phys. Controlled Fusion **50**, 055007 (2008).
[20] B. Scott, Phys. Plasmas **12**, 082305 (2005).
[21] O. Grulke, J. L. Terry, B. LaBombard, and S. J. Zweben, Phys. Plasmas **13**, 012306 (2006).
[22] J. M. Beall, Y. C. Kim, and E. J. Powers, J. Appl. Phys. **53**, 3933 (1982).
[23] B. LaBombard, J. W. Hughes, N. Smick, A. Graf, K. Marr, R. McDermott, M. Reinke, M. Greenwald, B. Lipschultz, J. L. Terry, D. G. Whyte, and S. J. Zweben, Phys. Plasmas **15**, 056106 (2008).
[24] B. D. Scott, A. Bottino, R. Hatzky, S. Jolliet, A. Kendl, B. F. McMillan, D. Reiser, and T. Ribeiro, in *Proceedings of the 22nd IAEA Fusion Energy Conference*, Geneva 2008 (IAEA, Vienna, 2009), Paper No. IAEA-CN-165/TH/P8-13.
[25] X. Q. Xu, R. H. Cohen, T. D. Rognlien, and J. R. Myra, Phys. Plasmas **7**, 1951 (2000).
[26] T. Ribeiro and B. Scott, Plasma Phys. Controlled Fusion **47**, 1657 (2005).